Interface Potentials Inside Solid-State Batteries: Origins and Implications

Yue Qi, Michael W. Swift, Elliot J. Fuller, A.Alec Talin

Affiliations of the Authors:

Yue Qi, School of Engineering, Brown University, Providence, Rhode Island 02912, United States; orcid.org/0000-0001-5331-1193; Email: yueqi@brown.edu

Michael W. Swift, Center for Computational Materials Science, U.S. Naval Research Laboratory, Washington, DC 20375, United States, orcid.org/0000-0003-2974-6052; Email: michael.swift@nrl.navy.mil

Elliot J. Fuller, Sandia National Laboratories, Livermore, California 94550, United States, orcid.org/0000-0001-7912-8688; Email: ejfull@sandia.gov

A. Alec Talin, Sandia National Laboratories, Livermore, California 94550, United States; orcid.org/0000-0002-1102-680X; Email: aatalin@sandia.gov

Abstract:

Interface resistance has become a significant bottleneck for solid-state batteries (SSBs). Most studies of interface resistance have focused on extrinsic mechanisms such as interface reactions and imperfect contact between electrodes and solid electrolytes. Interface potentials are an important intrinsic mechanism that is often ignored. Here, we highlight Kelvin probe force microscopy (KPFM) as a tool to image the local potential at interfaces inside solid-state batteries, examining the existing literature and discussing challenges in interpretation. Drawing analogies with electron transport in metal/semiconductor interfaces, we showcase a formalism that predicts intrinsic ionic resistance based on the properties of the contacting phases, and we emphasize that future battery designs should start from material pairs with low intrinsic resistance. We conclude by outlining future directions in the study of interface potentials through both theory and experiment.

Keyword: interface; predictive modeling, transportation, energy storage

Conflict of Interest Statement: On behalf of all authors, the corresponding author states that there is no conflict of interest.

Intrinsic and Extrinsic Interface Resistance

Solid State Batteries (SSB) rely on ionic transport through physically contacted interfaces. With the increasing ionic conductivity and shrinking thickness of the solid electrolytes (SE),[1-6] ion transport within the SE is no longer the rate-limiting step in many current SSB designs. Instead, high resistance at the interfaces has become the bottleneck and an important remaining challenge to overcome.[7-9] Interface resistance is often attributed to imperfections, such as SE interphases resulting from decomposition of thermodynamically unstable SE/electrode interfaces [8, 10, 11] and the lack of intimate contact between the electrodes and the SE. [12 13] A more fundamental question is, *"What is the distribution of potentials at an atomically connected, thermodynamically stable interface, and how does it drive the transport of ions?"*

Analogies can be made with electron (or hole) transport at metal/semiconductor interfaces. The Schottky barrier theory[14] describes the barrier for e^-/h^+ transport based on the work function difference between the metal and the semiconductor together with the semiconductor electron affinity. Although the contact area, presence of impurities, possible interface reactions, and grain orientation details can modify the *extrinsic* barrier, the theory points to an underlying *intrinsic* resistance. [15] As a result, one can identify combinations of materials most suited for a given type of contact: either low-resistance Ohmic contacts (such as those used to make source and drain contacts for transistors) or rectifying contacts for high-quality diodes, critical to the development of modern electronics and information technology. [14]

Borrowing from semiconductors, can we similarly construct a formalism to predict the intrinsic interface resistance for ion transport in SSBs based only on the two contacting phases (i.e. the solid electrolyte and electrode)? With this information, further improved SSB designs should only use materials whose interfaces have low *intrinsic* interface resistance, so that mitigation of *extrinsic* interface resistances (enhancing wetting, increasing contact area, eliminating phases limiting ion transport, …) can result in a battery with improved performance. Therefore, measurement and calculation methods to quantify the *intrinsic* resistance for a given pair of electrode and solid-electrolyte materials are needed for comparing and designing SSB systems.

Intrinsic interface resistance would arise even at a pristine interface with perfect contact and without interphase formation. Here, electrons (or holes) and ions redistribute at heterogeneous interfaces causing an intrinsic electrostatic potential difference, analogous to the electronic heterogeneous metal/semiconductor interfaces [15] and the "space-charge layer" in ionic conductors. [16, 17] While low Li-ion migration barriers in neutral solid-electrolyte materials enable fast ionic conductivity,[18, 19] the Li-ion transfer rates across a charged electrode/solid-electrolyte interface can be substantially affected. The electric field created by the interface potential drop ($d\phi/dx$) in the SE near the interface may accelerate or hinder Li^+ ion migration toward the interface, as illustrated in **Fig 1**. Further, the charge-transfer reaction $Li^0_\alpha \rightleftharpoons Li^+_{SE} + e^-_\alpha$ refers to the process in which the Li-ions in the solid electrolyte (e.g. Li^+ as interstitials in the SE) neutralize with the electrons on the electrode (e^-) to become Li atoms, Li^0, inserted either on the surface of a Li-metal or into the lattice of a host electrode (e.g. Si or $LiCoO_2$). In these electrodes, the Li ion and its hosting site can be jointly viewed as the Li^0_α, as $Li^0_\alpha = [Li^+ - Site^-]$.[20] An overpotential across the electrode/SE interface is required to overcome these barriers and dictates the overall charge transfer kinetics. [21 22] Thus, probing the electrical potential variation inside the SSB would provide insight into the intrinsic nature of the interface and inform the construction of models similar to the semiconductor case.

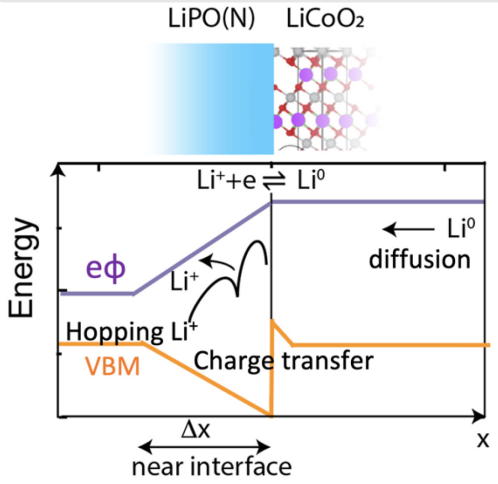

Fig 1: Mechanisms for charge transport and transfer at solid-state electrochemical interfaces. The electronic energy alignment will affect the near-interface phenomena due to the electrical potential gradient $d\phi/dx$. The VBM (not to scale) indicates band bending at the interface, emphasizing the coupled ionic-and-electronic degrees of freedom at these interfaces.

KPFM Measurement for SSB

Recently, Kelvin probe force microscopy (KPFM) has emerged as a technique for imaging the electrical potential variation in SSBs. KPFM measures the contact potential difference (CPD) between an atomic force microscopy (AFM) tip and the surface. If the tip work function is assumed constant and under ideal conditions, CPD maps reflect variations in the specimen work function, and thus have been extensively used to characterize metals and semiconductors.[23] KPFM has also been applied to SSB, along with other *in situ* and *operando* probing techniques.[24] For individual SE materials, Song et al. used KPFM to scan deposited LiPON films with different dopants and interpreted the CPD as the "intrinsic work function" of doped LiPON. [25] However, this interpretation of KPFM relies on hidden assumptions which do not hold in the SSB context. Challenges in interpretation arise when the SSB is formed, charged, and cycled, because of the additional applied potentials and changes in the electrode work functions when ions are transferred, as we discuss in detail in this article. Currently, KPFM measurements have been successfully correlated with other techniques to provide insights into internal SSB dynamics, but a consensus framework for the quantitative interpretation of KPFM measurements themselves has yet to emerge.[6, 7]

In this work, we begin by reviewing several key examples of KPFM measurements in SSBs. We then proceed to provide our own analysis to interpret these data quantitatively. **Fig 2a** shows the KPFM schematics by Masuda et al., who assembled an SSB with a cathode of $LiCoPO_4$ (LCP) combined with Pd metal and the solid electrolyte $Li_{1+x}Al_xTi_{2-x}(PO_4)_3$ (LATP). They directly visualized the CPD map in different particles and noted changes during charging. By overlapping KPFM with SEM images, Pd was identified as having the lowest CPD values before charging. After charging the battery to a higher voltage, the CPD values at all places increased, and they believed Li ions were depleted even in LATP SE during charging. The KPFM-measured CPD was called "internal electrical potential" in the analysis.[26] More recently, Otoyama et al. combined KPFM with scanning spreading resistance microscopy (SSRM) [27] to directly visualize the local electronic properties of individual $LiNi_{1/3}Mn_{1/3}Co_{1/3}$ (NMC) particles embedded in $75Li_2S$-$25P_2S_5$ (mol %) glass SEs as the composite cathode in an SSB. They added the OCV voltage to the KPFM-

measured CPD profile and the combined CPD for individual electrode particles showed an increase of about 1 V after charging.

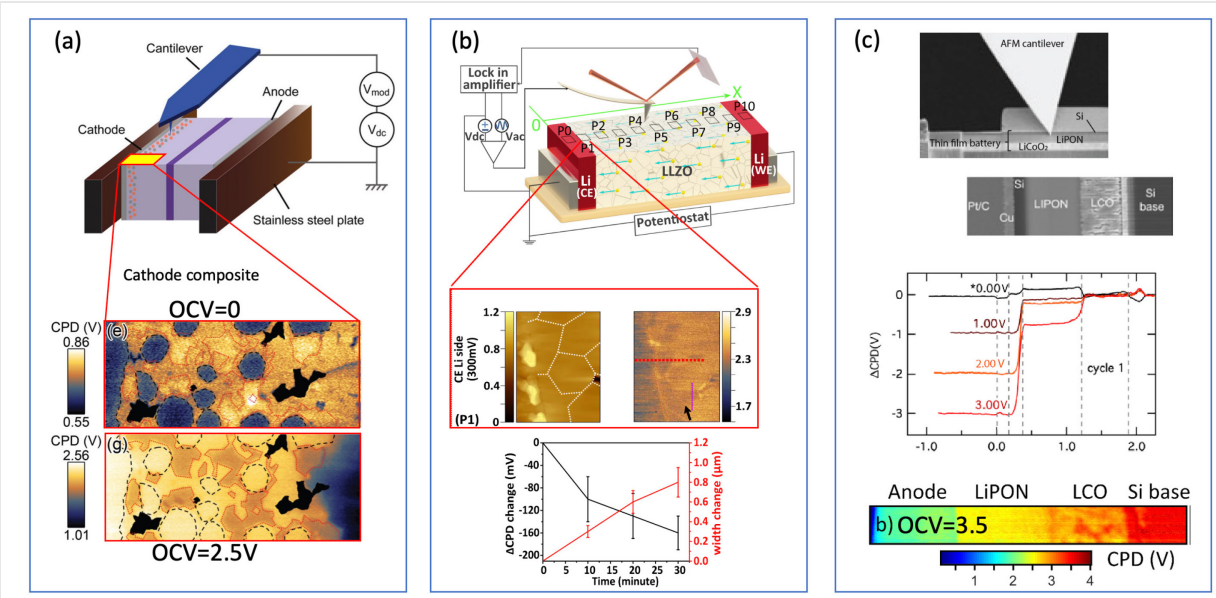

Fig 2: Schematic of KPFM in SBB. (a) Masuda et al.'s set up to map CPD of cathode composite (in the yellow box) at two OCV states.[26] (b) Zhu et al.'s set up to observe CPD maps on the LLZO surface of a symmetric Li/Al-doped-LLZO/Li cell during battery cycling. The CPD map in Box P1 at two states are shown. The bottom figure tracks the time evolution of the ΔCPD and width change as a function of plating time under 300 mV along the line parallel to the electrode surface.[29] (c) Fuller's setup for thin film SSB. The line averaged ΔCPD with respect to the OCV=0 state is shown in the middle figure and the bottom figure is the CPD map at OCV = 3.5V.[31]

To obtain more dynamic information during cell-charge discharge, Masuda et al. further measured CPD images during cyclic voltammetry scan in a similar setup shown in **Fig 2a**. They estimated that the difference in cell voltage between the first and last scan lines of a CPD image was ~24 mV because the acquisition of a CPD image took ~4 min.[28] Recently, the local time-dependent CPD map was obtained *in situ* for a $Li/Li_{6.25}Al_{0.25}La_3Zr_2O_{12}/Li$ symmetric cell by Zhu et al., as shown in **Fig 2b**.[29] The Li counter electrode (Li-CE, plating side) features a lower CPD value (≈2.1 V) compared to LLZO (≈2.35 V). The CPD values of the LLZO near the stripping side increased and the step-like decrease in CPD for some LLZO grains (purple dotted line in **Fig 2b**) near the plating interface decreases with the Li-plating time. These changes correlate well with the electron-accumulation-induced Li plating near specific LLZO grain boundaries.[30] They described the CPD changes in the LLZO phase is equivalent to the "Galvani potential" changes in the LLZO phase. This interpretation will get more complicated when analyzing full-cell CPD maps.

Some of the authors in this article (Fuller et al.) have deposited a thin film battery with Si/LiPON/$LiCoO_2$ sandwiched between Cu and Pt current collectors followed by C/Pt and Si substrates on both sides, respectively (**Fig 2c**). They measured the CPD across all the layers inside of an SSB at different OCV conditions after charge and discharge cycles. They quantified the potential profile in each layer and their changes at the corresponding OCV conditions.[31]

KPFM Interpretation for Neutral and Charged Surfaces

Here we reiterate some key derivations and definitions to illustrate how to quantitatively interpret the CPD profile in SSB. The KPFM-measured raw CPD_{tip} images the Volta potential difference between the sample surface and the tip. For charge-neutral materials, this is equivalent to the work function, Φ, which is more typically used in the literature.[23]

$$CPD_{tip} = \frac{\Phi_{\text{tip}} - \Phi_{\text{sample}}}{e}. \quad (1)$$

Here Φ_{sample} is the local work function, Φ_{tip} is the work function of the scanning probe tip, e is the elementary charge. If two samples are isolated and charge neutral (**Fig 3a**), their work function difference can be obtained by the CPD difference, as

$$\Delta CPD_{1-2} = \frac{\Phi_{\text{tip}} - \Phi_1}{e} - \frac{\Phi_{\text{tip}} - \Phi_2}{e} = \frac{\Phi_2 - \Phi_1}{e} = \Delta\Phi_{2-1} \quad (2)$$

When the surfaces are charged (e.g. due to band-bending when forming an interface or charged in SSB assembly), additional terms are introduced. In solid-state physics, a local vacuum level, E_{vac}^{loc}, is typically used when discussing charged surfaces. In electrochemistry, a constant global vacuum level E_{vac}^{glob} is used and a Volta potential, ψ, is defined for a charged surface, as $E_{vac}^{loc} = -e\psi$. The inner energy level, given by E_{in}, is also the Galvani potential ($E_{in} = -e\varphi$). μ_e is the chemical potential of electrons in a pristine material (charge-neutral), and χ is the surface dipole term, which can substantially modify the work function. In this work, both the Fermi energy and the electrochemical potential of electrons in material refer to the charge-neutral state ($E_F = \tilde{\mu}_e$). The work function is the energy difference between the Fermi energy and the local vacuum level. By these definitions, the following relationships hold true:

$$\Phi \equiv E_{vac}^{loc} - E_F = -e\psi - \tilde{\mu}_e \quad (3)$$

$$\tilde{\mu}_e \equiv \mu_e - e\varphi \quad (4)$$

The KPFM tip will sense the contribution of the surface dipole (χ) and the electrons chemical potential (μ_e), as

$$\Phi = e\chi - \mu_e \quad (5).$$

Combining **Eqs 3, 4** and **5** connects the Galvani potential, Volta potential and the surface dipoles.

$$\varphi = \chi + \psi \quad (6)$$

The surface term χ can change significantly during battery operation, adsorption of gases, and other electrochemical or physical surface processes, affecting Φ and CPD. For this reason, to ensure stable and reproducible CPD measurements, most KPFM measurements are performed in

the clean environment of a vacuum chamber. Therefore, in more general terms, the KPFM collected *operando* $\mathrm{CPD}(x,y)_{tip}$ images are the Volta potential difference,

$$CPD(x,y)_{tip} = \frac{\Phi_{\mathrm{tip}} - \Phi(x,y)}{e} - \frac{\tilde{\mu}_e(x,y)}{e} \quad (7).$$

Here $\Phi(x,y)$ is the local work function and $\tilde{\mu}_e(x,y)$ is the electrochemical potential of electrons relative to the instrument ground.[32] According to **Eq 6**, if the surface dipole is the same, measuring the Volta potential change can indicate the Galvani potential change, as shown in **Fig 2b**.[29]

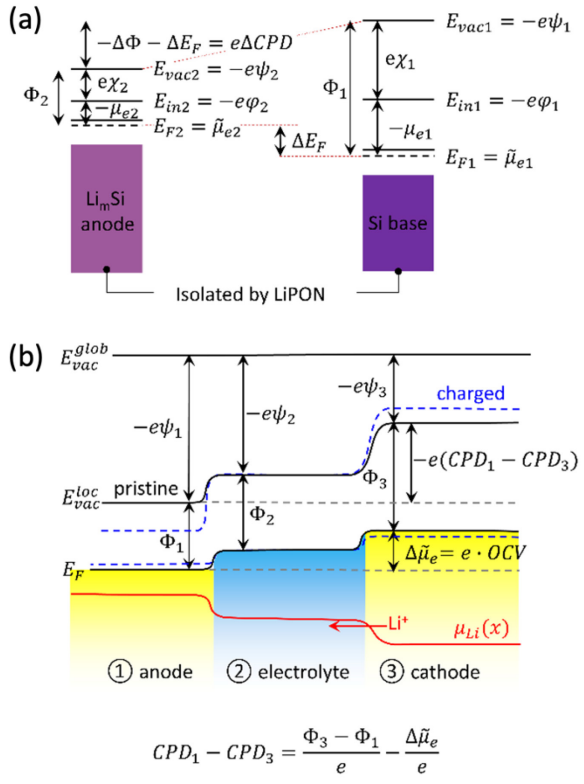

Fig 3. Extended electronic band diagrams to illustrate what KPFM is measuring. Reproduced from Fuller et al. [30] (a) the band diagram of the Li_mSi anode and Si base, showing that the CPD difference between the two is equal to the sum of the differences in work function ($\Delta\Phi$) and Fermi energy (electrochemical potential of electrons: $\Delta E_F = \Delta\tilde{\mu}_e$) after anode lithiation. Their Fermi levels are not aligned as the two materials are separated by an electronically insulating solid electrolyte. (b) Generalized band diagram structure of a SSB showing how the KPFM-measured CPD difference between the cathode and anode depends on the Φ and $\tilde{\mu}_e$ in these materials. Global vacuum level at infinite distance is also shown. As the battery is charged, both the Fermi level and work function (and surface term) of materials change as a function of lithium concentration, as indicated by the blue dashed lines.

KPFM Interpretation for SSBs

The electrochemical potential of electrons, $\tilde{\mu}_e$, (or more precisely, the voltage V which is equal to $-\tilde{\mu}_e/e$) serves as the electromotive force of a battery, and its distribution inside an SSB can reveal locations of high resistance. One would like to extract $-\tilde{\mu}_e(x,y)/e$ from the $\mathrm{CPD}(x,y)_{tip}$ images collected *operando* at various open circuit voltages (OCVs) during charge-cycling. In the example of **Fig 2c**, x was set to be the anode/SE/cathode direction and $\mathrm{CPD}(x,y)_{tip}$ was averaged along the y direction. The obtained $\mathrm{CPD}(x)$ can be compared to 1D SSB model that describes the potential drops across different electrode and electrolyte layers.

The chemical potential of neutral Li (μ_{Li}) and the electrochemical potential of Li^+ ions ($\tilde{\mu}_{Li^+}$) are also connected with $\tilde{\mu}_e$ in SSBs via the band diagram schematically shown in **Fig 3**. The two

electrodes are separated by the electronically insulating solid electrolyte layer, so their Fermi levels, E_F, are not aligned to the same level. Instead, under equilibrium (OCV) conditions, Li^+ ions will flow across the interface, shifting μ_{Li} until $\tilde{\mu}_{\mathrm{Li}^+}$ becomes a constant (the condition for electrochemical equilibrium). This constant value can be used as a zero reference: $\Delta\tilde{\mu}_{Li^+}(x) = -\Delta\tilde{\mu}_e(x) + \Delta\mu_{\mathrm{Li}}(x) = 0$, therefore $\Delta\tilde{\mu}_e(x) = \Delta\mu_{\mathrm{Li}}(x)$, where μ_{Li} is the chemical potential of Li.[16] A generalized band-diagram theory for SSBs has been developed to depict the electrochemical potential driving force causing Li^+ ions and e^-/h^+ accumulation at the interfaces, shifting the $\tilde{\mu}_{\mathrm{Li}^+}$ and the electric potential $e\phi$, and aligning the band structures. This theory allows prediction of $\Delta\Phi(x)$ and $\Delta\tilde{\mu}_e(x)$ based on the equilibrium condition.[16]

The KPFM-measured CPD difference between the cathode and anode depends on the Φ and $\tilde{\mu}_e$ in these materials, according to **Eq. 7**. As the battery is charged, both the Fermi level and work function (and surface term) of these materials change as a function of lithium concentration, as indicated in **Fig 4**. Therefore, interpreting the measured CPD data must consider the substantial changes in both $\Phi(x,y)$ and $\tilde{\mu}_e(x,y)$ as a function of the state of charge (SOC). Furthermore, Because Φ_{tip} may change over time due to interaction with electrochemically active battery layers (e.g. lithiation of the tip was observed by Fuller et al.), it is preferred to use an inert material in the SSB, e.g. an inert Si electrode base that is not going to be lithiated, as the reference (Φ_{base}) for $CPD(x)$ profile:

$$CPD(x)_{base} = CPD(x) - CPD_{base} = \frac{\Phi(x)-\Phi_{base}}{\mathrm{e}} - \frac{\tilde{\mu}_e(x)-\tilde{\mu}_{e_{base}}}{e} \quad (8)$$

Although the surface and bulk potentials may not be the same, since the surface and the bulk are continuously connected, the change in CPD (surface potential change) is often assumed to be equal to the change in the bulk potential. This assumption can be invalid sometimes, for example, Fuller et al. observed higher lithium concentration on the surface of Si electrode at high lithiation levels. Such a situation can be included naturally if the corresponding changes in the work function Φ and surface term χ are known.

Comparing $CPD(x)$ at SOC, the *operando* information is obtained:

$$\Delta\mathrm{CPD}(x) = \mathrm{CPD}(x)_{base}^{SOC} - \mathrm{CPD}(x)_{base}^{SOC=0} = \frac{\Delta\Phi(x)}{e} - \frac{\Delta\tilde{\mu}_e(x)}{e} \quad (9),$$

which reflects changes $\Delta\Phi$ and $\Delta\tilde{\mu}_e$ relative to the OCV = 0.0 V state. If the work functions $\Delta\Phi(x)$ and Φ_{base} remain independent of the SOC, we can further extract $-\tilde{\mu}_e(x,y)/e$ by subtracting the $\Delta CPD(x)$ profile recorded at $-\frac{\tilde{\mu}_e(x,y)}{e} = 0\ V$ (cathode and anode grounded, or SOC=0) from the CPD profiles measured in other SOC, $-\frac{\tilde{\mu}_e(x)}{e} = \Delta\mathrm{CPD}(x)$. However, this assumption can quickly become invalid, as the work function of the electrode materials, as well as other electronic properties, varies with the lithium concentration (or the SOC). Lithiation of an electrode can change both the Fermi level and the work function. This can be easily observed in Density Functional Theory (DFT) predicted material properties, as shown in **Fig 4**: the work function, Φ of Li_mSi changes dramatically with lithium concentration m, but the work function of LCO shows a much smaller change with lithium content.

In **Fig 2c**, $\mathrm{CPD}(x)_{base}^{SOC=0}$ is plotted for the anode and cathode grounded at OCV = 0 V (shown in black). Under these conditions $\tilde{\mu}_e = 0$ in the electrodes, and therefore CPD(x) is proportional to only the local work function of SSB layers $\Phi(x)$. CPD(x) is mainly flat in each layer, consistent with a uniform composition inside each layer, with sharp drops occurring at the LCO-LiPON and Si-LiPON interfaces. Interface-formation-induced work function change has been captured at the LCO-LiPON interface, where a small peak on the LiPON side and a dip on the LCO side suggests Li^+ transfer from LCO to LiPON. Schwöbel et al. experimentally observed a decrease of 0.25 eV in the LCO work function upon deposition of LiPON on LCO(5) which is consistent with the CPD difference of (0.257 ± 0.065) V and DFT-informed band diagram prediction. [16]

Fig 2c also showed the $\Delta\mathrm{CPD}(x)$ profiles for OCV values of 1.0 V, 2.0 V, and 3.0 V, after subtracting the OCV = 0.0 V profile, shows that ΔCPD(x) between the Cu current collector and the Pt current collector (or Si base) is equal to the measured OCV of the cell and which is equal to the differences in $\Delta\tilde{\mu}_e/e$. This result is expected for the case of electrodes that do not undergo Li insertion/extraction during charge-cycling and, therefore, do not undergo changes in work function ($\Delta\Phi = 0$).

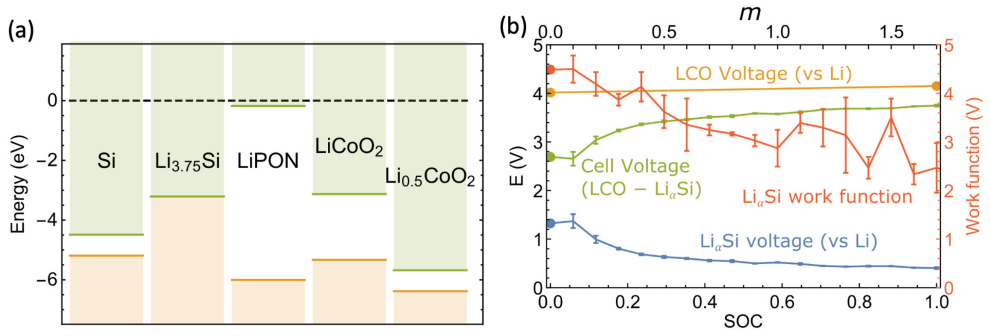

Fig 4 DFT computed properties varying with the state of charge (SOC). (a) The band structure (orange: valence bands and green: conduction bands) for the electrode's materials at two lithiated states and the solid electrolyte LiPON. All the materials are pristine (not charged, not connected). The zero is the vacuum level. The work function for the electrode materials is the energy difference between the valence band maximum and zero. (b) the calculated work function of Li_mSi (shown in red with uncertainty bars for the same ensemble) decreases with lithium content, m, which is shown on the top axis. The potential of the negative electrode Li_mSi vs. Li is shown in blue, positive electrode potential vs. Li is shown in orange (going from $LiCoO_2$ to $Li_{0.5}CoO_2$), and the full cell voltage is shown in green. (Figure adopted from the Supporting Information of Ref 31)

However, for the $\Delta\mathrm{CPD}(x)$ profiles during further charging, by increasing the voltage differences to drive the lithium transport from LCO to Si, shown in **Fig 5,** the SSB layers undergo significant change in Li content, and $\Delta\tilde{\mu}_e$ is convolved with changes in ΔΦ. At OCV = 3.35 V, nearly the

entire width of the Si anode has a CPD higher than OCV, indicating that the negative electrode (Si) has become lithiated, resulting in changes in $\Delta\Phi$. Li insertion is confirmed both by an increase in topographical height due to volume expansion and by the NDP profile which quantifies the lithium concentration. Further, the current collector was found to be lithiated [33, 34] as the lithium front slowly moved into the Cu electrode and further into the Pt/C support structure from OCV = 3.35 V to 4.0 V.

To deconvolute the SOC-dependent $\Delta\mathrm{CPD}(x)$, $\Delta\tilde{\mu}_e(x)$, and $\Delta\Phi(x)$ profiles, a DFT-informed band-diagram model, which was previously developed by Swift and Qi,[16, 31] was used to simulate $\Delta\mathrm{CPD}(x)$. The DFT-computed materials properties (as shown in **Fig 4**) were aligned to give the electronic bands, chemical potentials, electrochemical potentials, and inner (Galvani) electrostatic potentials for the entire SSB, following the protocol developed by Swift and Qi. [16, 35, 36]The simulated $\Delta\mathrm{CPD}(x)$ based on the internal energy diagram at different OCVs is obtained in **Fig 5b**.

The resulting calculated values are in good agreement with the KPFM data although the chemistry of the modeled solid electrolyte is not identical to those of the measured cells (**Fig. 5**). In the current collectors far from the cell, the work function is unchanged and $\Delta\mathrm{CPD}(x)$ is equal to $-V_{\mathrm{OCV}}$. From 0 V to 3 V, the lithiation of the silicon electrode is minimal and the work function change is negligible; the $\Delta\mathrm{CPD}(x)$ between silicon and LCO is equal to $-V_{\mathrm{OCV}}$. As Si begins to substantially lithiate, the work function change (red curve in **Fig. 4**) outpaces the voltage change (blue curve in **Fig. 4**). This causes a higher $\Delta\mathrm{CPD}(x)$ in $\mathrm{Li}_m\mathrm{Si}$ at OCV = 3.75 V compared to OCV = 3.0 V. This agrees well with the experimental results. Lithiation extends into the current collector, keeping the $\Delta\mathrm{CPD}(x)$ high. Past the lithiation front, the work function of the current collector returns to its pristine value, and the $\Delta\mathrm{CPD}(x)$ again matches $-V_{\mathrm{OCV}}$.

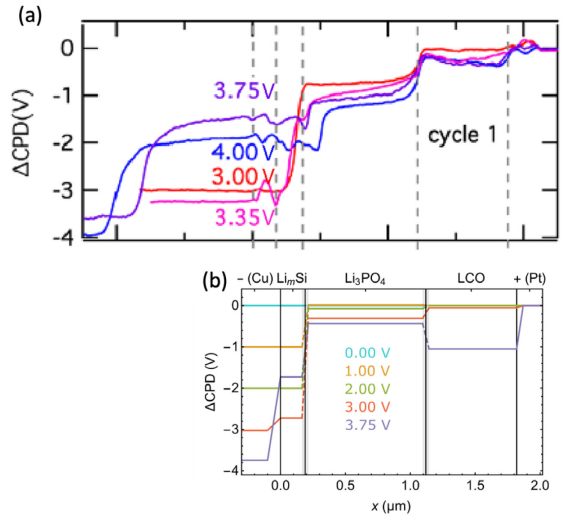

Fig 5 (a) experimentally measured $\Delta\mathrm{CPD}$ after lithiation started and (b) simulated $\Delta\mathrm{CPD}$ with respect to SOC=0 at different OCV conditions for the SSB shown in **Fig 2c.** (Figure adopted from the experimental and modeling results in Ref 31)

While the interface potential drop in experiments is clear, its variation with the cell voltage is quite complex. It is still difficult to quantify the measurements, even by correlating with other probing techniques, as shown in other examples in **Fig 2**. This is because the CPD contains the work function (Φ) and the electrochemical potential of electrons ($\tilde{\mu}_e$), as shown in **Eq. 7**. While the work function (at charge neutral state) of each material in the SSB is defined, it also varies with Li-concentration. **Fig 5** underscores the importance of the bidirectional development of modeling and experiments.[31] In this example, the KPFM measures ΔCPD (**Fig 5a**), the DFT-informed band-diagram model successfully quantifies the Φ and $\tilde{\mu}_e$ contributions both separately and jointly (**Fig 5b**). Importantly, the agreement between the experiments and modeling allowed clarification of this relationship, shown in **Eq. 7,** , and deconvolute the complex relationship between the SOC-dependent interface potential drop, which does not change monotonically with the SOC of the SSB. Another advantage of comparing the KPFM data with the band diagram is that the measured CPD only contains electronic properties (e.g. work function). The band diagram includes all the other information, e.g. the chemical potential of the Li atom and the electrochemical potential of Li^+, as well as the electric potential. Validating the predicted CPD suggests that other predictions are likely to be correct and can be used to model device performance.

Furthermore, Fuller et al. have demonstrated that large interface potential drop is correlated with the interface resistance measured from traditional electrochemical impedance spectroscopy (EIS) following battery cycling, indicating the rate-limiting process.[37] Although the reason for this correlation is still derived and its generalization needs to be tested, the connection from theory and modeling to battery performance, promises new opportunities to computationally screen materials and directly design interfaces for SSB. With the increasing number of SE and electrode materials being developed, a computational interface design tool is inevitably necessary, as the number of interfaces and the number of SSB configurations scale as N^2 and N^3, respectively, with the number of materials (N). Swift et al. sampled 48 SSB configurations and identified multiple interfaces with low potential drop. [35]

Conclusions and Future Directions

Practical SSBs present significant experimental and theoretical challenges to the control of interface potentials due to their complexity. Model systems, such as symmetrical thin film batteries[7] and those incorporating epitaxial layers[38] could substantially reduce these challenges and therefore represent an important future direction for fundamental theory development. Symmetrical electrode/SE/electrode batteries, for example, could simplify interpretation of EIS data and characterization of the space-charge-layer. Epitaxial thin film SSBs can yield sharper interfaces and enable control over crystallographic orientation, which affects both ionic transport and local electronic structure (e.g. work function). Symmetric electrode/SE/electrode structures are also appealing because they exclude highly reactive lithiated anodes, which can form surface reaction layers even under high-vacuum conditions (condition as Fuller et al. found for lithiated Si or lithium metal vacuum chambers with even ~10^{-6} Pa of O_2).[31, 39]

Another important opportunity is to develop new (or adapt existing) methods to image potentials in SBBs that are easier to implement experimentally than KPFM and that could bring additional analytical capability. In the semiconductor and photovoltaics industries, methods based on scanning electron microscopy (SEM) such as electron beam induced current and voltage (EBIC, EBIV) [40] are used routinely to visualize local potentials and space-charge regions. An advantage of the SEM compared to KPFM is that it's less sensitive to surface topography and thus may not require careful polishing using a focused ion beam (which could compromise some samples). Other advantages of the SEM (as well as the transmission electron microscope) is that the electron beam can be used to locally probe the composition and electronic structure via techniques such as electron dispersive, cathodoluminescence, and electron energy loss spectroscopies, and could be modulated temporally, enabling time-dependent dynamic experiments that could compliment traditional electrochemical techniques such as galvanostatic intermittent titration and related methods.[41]

While the DFT-informed band-diagram model has been successful in interpreting KPFM data, further theoretical development is needed to achieve quantitative prediction of CPD(x) across a wider range of conditions. One important direction is the prediction of Fermi levels in SEs at all stages of the charge-discharge cycle. For a semiconductor in equilibrium, the concentrations of charged point defects and impurities are controlled by the Fermi level, resulting in Fermi level "pinning" within the gap at a position dictated by charge neutrality. Chemical potentials of relevant species are controlled by growth conditions, allowing the Fermi level to be tuned from *p*-type to *n*-type depending on the relative concentrations of dopants and/or native defects. DFT calculations of defect formation energies take these chemical potentials as input, and can predict the Fermi level accurately.[42] The situation becomes more complicated for SEs in SSB processing.[16] SEs are electrically insulating, so their Fermi level is within the band gap. However, charge neutrality no longer holds in the space-charge layers near SE/electrode interfaces.[36] Furthermore, the lithium chemical potential μ_{Li} changes dramatically during cycling, so it is governed not only by growth conditions, but also by the battery SOC and the cycling history. Under the "minimum interface" assumption, μ_{Li} is sloped in the bulk of the SE, going from the SE's lithium-rich stability limit near the anode to the lithium-poor stability limit near the cathode.[16] Under the "extrinsic control" assumption, μ_{Li} is fixed in the bulk of the SE, and its value is an empirical parameter that can vary with state of charge. Fuller et al. used this assumption, and found a flat Fermi level in their LiPON SE with only modest variation during cycling.[31] Further method development is needed to determine the dominant factors controlling the Fermi level in the SE bulk. Joint work with experiments in simplified model systems could lead to a predictive model for *a priori* calculation of the Fermi level.

These advances in model system characterization and band diagram modeling will further pave the road to connecting the interface potential drop and the charge transfer kinetics in SSB. The rate limiting step for charge transfer kinetics across SSB interfaces needs to be determined, so the *intrinsic* interface resistance can be predicted without requiring the interface to be made experimentally or simulated explicitly but based purely on the properties of the electrode and SE materials. Further stabilizing the interface and enhancing the contact area at the interfaces with

low intrinsic ion transfer resistance will help to solve the interface design challenges in solid state batteries. [43]

Acknowledgments

Y. Qi thanks for the helpful discussions with Prof. Jürgen Janek.

References

1. Janek, J.; Zeier, W. G., A solid future for battery development. *Nature Energy* **2016,** *1* (9), 16141-16141.
2. Dudney, N. J., Solid-state thin-film rechargeable batteries. *Materials Science and Engineering: B* **2005,** *116* (3), 245-249.
3. Dudney, N. J.; Li, J., Using all energy in a battery. *Science* **2015,** *347* (6218), 131-132.
4. Dudney, N. J.; West, W. C.; Nanda, J., *Handbook of Solid State Batteries*. WORLD SCIENTIFIC: 2015; Vol. 6.
5. Danilov, D.; Niessen, R. A. H.; Notten, P. H. L., Modeling All-Solid-State Li-Ion Batteries. *Journal of The Electrochemical Society* **2011,** *158* (3), A215-A222.
6. Zhang, Z.; Shao, Y.; Lotsch, B.; Hu, Y.-S.; Li, H.; Janek, J.; Nazar, L. F.; Nan, C.-W.; Maier, J.; Armand, M.; Chen, L., New horizons for inorganic solid state ion conductors. *Energy & Environmental Science* **2018,** *11* (8), 1945-1976.
7. Luntz, A. C.; Voss, J.; Reuter, K., Interfacial Challenges in Solid-State Li Ion Batteries. *The Journal of Physical Chemistry Letters* **2015,** *6* (22), 4599-4604.
8. Banerjee, A.; Wang, X.; Fang, C.; Wu, E. A.; Meng, Y. S., Interfaces and Interphases in All-Solid-State Batteries with Inorganic Solid Electrolytes. *Chemical Reviews* **2020,** *120* (14), 6878-6933.
9. Pervez, S. A.; Cambaz, M. A.; Thangadurai, V.; Fichtner, M., Interface in Solid-State Lithium Battery: Challenges, Progress, and Outlook. *ACS Applied Materials & Interfaces* **2019,** *11* (25), 22029-22050.
10. Zhu, Y.; He, X.; Mo, Y., First principles study on electrochemical and chemical stability of solid electrolyte–electrode interfaces in all-solid-state Li-ion batteries. *Journal of Materials Chemistry A* **2016,** *4* (9), 3253-3266.
11. Xiao, Y.; Wang, Y.; Bo, S.-H.; Kim, J. C.; Miara, L. J.; Ceder, G., Understanding interface stability in solid-state batteries. *Nature Reviews Materials* **2020,** *5* (2), 105-126.
12. Chen, X.; He, W.; Ding, L.-X.; Wang, S.; Wang, H., Enhancing interfacial contact in all solid state batteries with a cathode-supported solid electrolyte membrane framework. *Energy & Environmental Science* **2019,** *12* (3), 938-944.
13. Tian, H.-K.; Qi, Y., Simulation of the Effect of Contact Area Loss in All-Solid-State Li-Ion Batteries. *Journal of The Electrochemical Society* **2017,** *164* (11), E3512.
14. Sze, S. M.; Ng, K. K., *Physics of Semiconductor Devices*. John Wiley & Sons, Inc.: Hoboken, NJ, USA, 2006.
15. Brillson, L. J., *Contacts to Semiconductors - Fundamentals and Technology*. William Andrew Publishing/Noyes: 1993.
16. Swift, M. W.; Qi, Y., First-Principles Prediction of Potentials and Space-Charge Layers in All-Solid-State Batteries. *Physical Review Letters* **2019,** *122* (16), 167701-167701.

17. Yamamoto, K.; Iriyama, Y.; Asaka, T.; Hirayama, T.; Fujita, H.; Fisher, C. A. J.; Nonaka, K.; Sugita, Y.; Ogumi, Z., Dynamic Visualization of the Electric Potential in an All-Solid-State Rechargeable Lithium Battery. *Angewandte Chemie International Edition* **2010,** *49* (26), 4414-4417.
18. He, X.; Zhu, Y.; Mo, Y., Origin of fast ion diffusion in super-ionic conductors. *Nature Communications* **2017,** *8* (1), 15893-15893.
19. Wang, Y.; Richards, W. D.; Ong, S. P.; Miara, L. J.; Kim, J. C.; Mo, Y.; Ceder, G., Design principles for solid-state lithium superionic conductors. *Nature Materials* **2015,** *14* (10), 1026-1031.
20. Doyle, M.; Fuller, T. F.; Newman, J., Modeling of Galvanostatic Charge and Discharge of the Lithium/Polymer/Insertion Cell. *Journal of The Electrochemical Society* **1993,** *140* (6), 1526.
21. Hobold, G. M.; Lopez, J.; Guo, R.; Minafra, N.; Banerjee, A.; Shirley Meng, Y.; Shao-Horn, Y.; Gallant, B. M., Moving beyond 99.9% Coulombic efficiency for lithium anodes in liquid electrolytes. *Nature Energy* **2021,** *6* (10), 951-960.
22. Fraggedakis, D.; McEldrew, M.; Smith, R. B.; Krishnan, Y.; Zhang, Y.; Bai, P.; Chueh, W. C.; Shao-Horn, Y.; Bazant, M. Z., Theory of coupled ion-electron transfer kinetics. *Electrochimica Acta* **2021,** *367*, 137432-137432.
23. Melitz, W.; Shen, J.; Kummel, A. C.; Lee, S., Kelvin probe force microscopy and its application. *Surface Science Reports* **2011,** *66* (1), 1-27.
24. Wynn, T. A.; Lee, J. Z.; Banerjee, A.; Meng, Y. S., In situ and operando probing of solid–solid interfaces in electrochemical devices. *MRS Bulletin* **2018,** *43* (10), 768-774.
25. Song, X.; Yu, W.; Zhou, S.; Zhao, L.; Li, A.; Wu, A.; Li, L.; Huang, H., Enhancement of Mn-doped LiPON electrolyte for higher performance of all-solid-state thin film lithium battery. *Materials Today Physics* **2023,** *33*, 101037.
26. Masuda, H.; Ishida, N.; Ogata, Y.; Ito, D.; Fujita, D., Internal potential mapping of charged solid-state-lithium ion batteries using in situ Kelvin probe force microscopy. *Nanoscale* **2017,** *9* (2), 893-898.
27. Otoyama, M.; Yamaoka, T.; Ito, H.; Inagi, Y.; Sakuda, A.; Tatsumisago, M.; Hayashi, A., Visualizing Local Electrical Properties of Composite Electrodes in Sulfide All-Solid-State Batteries by Scanning Probe Microscopy. *The Journal of Physical Chemistry C* **2021,** *125* (5), 2841-2849.
28. Masuda, H.; Matsushita, K.; Ito, D.; Fujita, D.; Ishida, N., Dynamically visualizing battery reactions by operando Kelvin probe force microscopy. *Communications Chemistry* **2019,** *2* (1), 140.
29. Zhu, C.; Fuchs, T.; Weber, S. A. L.; Richter, F. H.; Glasser, G.; Weber, F.; Butt, H.-J.; Janek, J.; Berger, R., Understanding the evolution of lithium dendrites at Li6.25Al0.25La3Zr2O12 grain boundaries via operando microscopy techniques. *Nature Communications* **2023,** *14* (1), 1300.
30. Tian, H.-K.; Liu, Z.; Ji, Y.; Chen, L.-Q.; Qi, Y., Interfacial Electronic Properties Dictate Li Dendrite Growth in Solid Electrolytes. *Chemistry of Materials* **2019,** *31* (18), 7351-7359.
31. Fuller, E. J.; Strelcov, E.; Weaver, J. L.; Swift, M. W.; Sugar, J. D.; Kolmakov, A.; Zhitenev, N.; McClelland, J. J.; Qi, Y.; Dura, J. A.; Talin, A. A., Spatially Resolved Potential and Li-Ion Distributions Reveal Performance-Limiting Regions in Solid-State Batteries. *ACS Energy Letters* **2021,** *6* (11), 3944-3951.
32. Sadewasser, S.; Glatzel, T., *Kelvin probe force microscopy*. Springer: 2012; Vol. 48.
33. Dey, A. N., Electrochemical Alloying of Lithium in Organic Electrolytes. *Journal of The Electrochemical Society* **1971,** *118* (10), 1547-1549.
34. Rehnlund, D.; Lindgren, F.; Böhme, S.; Nordh, T.; Zou, Y.; Pettersson, J.; Bexell, U.; Boman, M.; Edström, K.; Nyholm, L., Lithium trapping in alloy forming electrodes and current collectors for lithium based batteries. *Energy & Environmental Science* **2017,** *10* (6), 1350-1357.
35. Swift, M. W.; Jagad, H.; Park, J.; Qie, Y.; Wu, Y.; Qi, Y., Predicting low-impedance interfaces for solid-state batteries. *Current Opinion in Solid State and Materials Science* **2022,** *26* (3), 100990-100990.
36. Swift, M. W.; Swift, J. W.; Qi, Y., Modeling the electrical double layer at solid-state electrochemical interfaces. *Nature Computational Science* **2021,** *1* (3), 212-220.

37. Fuller, E. J.; Gabaly, F. E.; Léonard, F.; Agarwal, S.; Plimpton, S. J.; Jacobs-Gedrim, R. B.; James, C. D.; Marinella, M. J.; Talin, A. A., Li-Ion Synaptic Transistor for Low Power Analog Computing. *Advanced Materials* **2017,** *29* (4), 1604310-1604310.
38. Takeuchi, S.; Tan, H.; Bharathi, K. K.; Stafford, G. R.; Shin, J.; Yasui, S.; Takeuchi, I.; Bendersky, L. A., Epitaxial LiCoO2 Films as a Model System for Fundamental Electrochemical Studies of Positive Electrodes. *ACS Applied Materials & Interfaces* **2015,** *7* (15), 7901-7911.
39. Yulaev, A.; Oleshko, V.; Haney, P.; Liu, J.; Qi, Y.; Talin, A. A.; Leite, M. S.; Kolmakov, A., From Microparticles to Nanowires and Back: Radical Transformations in Plated Li Metal Morphology Revealed via in Situ Scanning Electron Microscopy. *Nano Letters* **2018,** *18* (3), 1644-1650.
40. Schroder, D. K., *Semiconductor Material and Device Characterization, 3rd Edition*. Wiley-IEEE Press: 2015.
41. Ellis, S. R.; Bartelt, N. C.; Léonard, F.; Celio, K. C.; Fuller, E. J.; Hughart, D. R.; Garland, D.; Marinella, M. J.; Michael, J. R.; Chandler, D. W.; Liao, B.; Talin, A. A., Scanning ultrafast electron microscopy reveals photovoltage dynamics at a deeply buried p−Si/SiO_2 interface. *Physical Review B* **2021,** *104* (16), L161303-L161303.
42. Freysoldt, C.; Grabowski, B.; Hickel, T.; Neugebauer, J.; Kresse, G.; Janotti, A.; Van de Walle, C. G., First-principles calculations for point defects in solids. *Reviews of Modern Physics* **2014,** *86* (1), 253-305.
43. Nanda, J.; Wang, C.; Liu, P., Frontiers of solid-state batteries. *MRS Bulletin* **2018,** *43* (10), 740-745.

Authors Contributions

All authors discussed the focus of this perspective. YQ developed the first draft. All authors revised the manuscript.

Competing Interests

On behalf of all authors, the corresponding author states that there is no competing interests.

Data availability

Not applicable

FundingY. Qi acknowledges the support from the National Science Foundation under Grants No. DMR-2054441. E.J Fuller and A. A. Talin were supported by the US Department of Energy, Office of Science, Office of Basic Energy Sciences, under grant DE-SC0021070. The work at Sandia National Laboratories was supported by the Laboratory-Directed Research and Development (LDRD) program. Sandia National Laboratories is a multi-mission laboratory managed and operated by National Technology and Engineering Solutions of Sandia, LLC, a wholly owned subsidiary of Honeywell International Inc., for the U.S. Department of Energy's National Nuclear Security Administration under contract DE-NA-0003525.

Bio

Yue Qi is the Joan Wernig Sorensen Professor of Engineering at Brown University. She received her Ph.D. from Caltech in 2001. She spent the next 12 years working at General Motors and transitioned back to academia in 2013 as a faculty member at Michigan State University before joining Brown in 2020. She develops multi-scale simulation methods, starting from quantum mechanics, to design materials and interfaces for energy efficiency and sustainability. She has served in multiple inaugural roles aimed at increasing diversity in Engineering. She can be reached at yueqi@brown.edu.

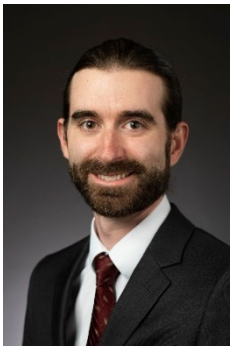

Michael Swift is a Research Physicist in the Center for Computational Materials Science at the US Naval Research Laboratory in Washington, DC. He received his PhD degree in physics from the University of California, Santa Barbara, in 2018, and his BS degree in physics from Rice University in Houston TX in 2013. His research interests include first-principles and multiscale modeling of materials for energy applications, especially light emission and energy storage. Swift can be reached by email at michael.swift@nrl.navy.mil .

Elliot J. Fuller is a staff member in the Materials Physics Department at Sandia National Laboratories. While formally trained as a physicist, he has a background in scanning probe microscopy, electrochemistry and nanoelectronics. Some of his current research interests include the study of model electrochemical systems including epitaxial thin films, electrochemical devices for brain inspired computing applications and the physics of strongly correlated oxides. He is a member of the American Physical Society, the Materials Research Society and the Electrochemical Society. He can be reached at ejfull@sandia.gov.

A. Alec Talin received Ph.D. in Materials Science and Engineering from UCLA in 1995. He is a Senior Scientist at Sandia National Laboratories, an Adjunct Associate Professor of Materials Science at the University of Maryland, College Park, and a Fellow of the American Physical Society. Prior to joining Sandia, Alec spent 6 years at Motorola Labs and 3 years (2009-12) as a project leader at the National Institute of Standards and Technology in Gaithersburg, MD. His interests focus on nanoelectronics and nanoionics, with applications to emerging computing technology, energy conversion, energy storage, and national security. He can be reached at aatalin@sandia.gov.